TISSUE ENGINEERING: Part C
Volume 29, Number 7, 2023

DOI: 10.1089/ten.tec.2023.0093

termis
Tissue Engineering
& Regenerative Medicine
International Society

RESEARCH ARTICLE

Regenerative Engineering of a Biphasic Patient-Fitted Temporomandibular Joint Condylar Prosthesis

David S. Nedrelow, DDS, MS,[1,2] Ali Rassi, MS,[3] Boushra Ajeeb, MS,[1] Cameron P. Jones,[2] Pedro Huebner, PhD,[3] Fabio G. Ritto, DDS, MD, MS, PhD,[4] Wendy R. Williams, DVM, MS,[5] Kar-Ming Fung, MD, PhD,[6] Bradford W. Gildon, MA, BSRT, RT(R),[7] Jakob M. Townsend, PhD,[1] and Michael S. Detamore, PhD[1]

Regenerative medicine approaches to restore the mandibular condyle of the temporomandibular joint (TMJ) may fill an unmet patient need. In this study, a method to implant an acellular regenerative TMJ prosthesis was developed for orthotopic implantation in a pilot goat study. The scaffold incorporated a porous, polycaprolactone-hydroxyapatite (PCL-HAp, 20wt% HAp) 3D printed condyle with a cartilage-matrix-containing hydrogel. A series of material characterizations was used to determine the structure, fluid transport, and mechanical properties of 3D printed PCL-HAp. To promote marrow uptake for cell seeding, a scaffold pore size of $152 \pm 68\,\mu m$ resulted in a whole blood transport initial velocity of $3.7 \pm 1.2\,mm \cdot s^{-1}$ transported to the full 1 cm height. The Young's modulus of PCL was increased by 67% with the addition of HAp, resulting in a stiffness of 269 ± 20 MPa for etched PCL-HAp. In addition, the bending modulus increased by 2.06-fold with the addition of HAp to 470 MPa for PCL-HAp. The prosthesis design with an integrated hydrogel was compared with unoperated contralateral control and no-hydrogel group in a goat model for 6 months. A guide was used to make the condylectomy cut, and the TMJ disc was preserved. MicroCT assessment of bone suggested variable tissue responses with some regions of bone growth and loss, although more loss may have been exhibited by the hydrogel group than the no-hydrogel group. A benchtop load transmission test suggested that the prosthesis was not shielding load to the underlying bone. Although variable, signs of neocartilage formation were exhibited by Alcian blue and collagen II staining on the anterior, functional surface of the condyle. Overall, this study demonstrated signs of functional TMJ restoration with an acellular prosthesis. There were apparent limitations to continuous, reproducible bone formation, and stratified zonal cartilage regeneration. Future work may refine the prosthesis design for a regenerative TMJ prosthesis amenable to clinical translation.

Keywords: goat, chondrogenic, osteogenic, 3D printed, polycaprolactone, hydroxyapatite

Impact Statement

The impact of this study is its translational approach to temporomandibular joint (TMJ) tissue engineering. Specifically, inspiration from the only FDA-approved custom TMJ prosthesis (TMJ Concepts/Stryker) was uniquely infused into an

[1]Stephenson School of Biomedical Engineering, University of Oklahoma, Norman, Oklahoma, USA.
[2]College of Dentistry, University of Oklahoma Health Sciences Center, Oklahoma City, Oklahoma, USA.
[3]School of Industrial and Systems Engineering, University of Oklahoma, Norman, Oklahoma, USA.
[4]Department of Oral and Maxillofacial Surgery, University of Oklahoma Health Sciences Center, Oklahoma City, Oklahoma, USA.
[5]Division of Comparative Medicine, University of Oklahoma Health Sciences Center, Oklahoma City, Oklahoma, USA.
[6]Department of Pathology, University of Oklahoma Health Sciences Center, Oklahoma City, Oklahoma, USA.
[7]Department of Medical Imaging and Radiation Sciences, University of Oklahoma College of Allied Health, Oklahoma City, Oklahoma, USA.

acellular design for a biphasic device to be an ''off-the-shelf'' approach to regenerate the mandibular condyle. Such a prosthesis would offer an alternative for TMJ patients with condylar fractures or with pediatric reconstruction needs, where current alloplastic devices may be limited. The current study was a pilot study, and helped to identify limitations in the design and to thus inform future work.

Introduction

The temporomandibular joint (TMJ) is essential to many daily life functions such as speaking, laughing, mastication, and upper-airway support. Although TMJ disease prevalence is high, affecting up to 12% of the overall population,[1,2] treatment with a TMJ total joint prosthesis is indicated only for a select patient population of the ~1 in 800 who have open surgery.[3,4] Inflammatory TMJ arthritis, recurrent fibrous and/or bony ankylosis, failed autogenous or alloplastic reconstruction, resorption, and trauma are among indications for a TMJ prosthesis.[5–7] Current TMJ prosthesis biomaterials cannot accommodate pediatric patient growth, and may not be appropriate for patients with metal hypersensitivities.[8,9] Therefore, regenerative medicine approaches are actively being investigated to develop a prosthesis capable of mandibular condylar tissue regeneration.[10,11]

TMJ animal models range from small, such as mouse or rabbit, to large, such as goat or Yucatan minipig.[12–16] Goat TMJ disc attachments to the condyle are similar to human disc attachments with medial and lateral collateral ligaments.[17] Zhu et al.[18] examined coronoid process donor tissue to reconstruct the mandibular condyle of goats. The Almarza group has performed a range of studies to establish baseline knowledge of the goat's TMJ tissue structures and behaviors.[15,19]

Both prevascularized and dual perfusion bioreactor-incubation regenerative medicine approaches have recently been pursued for TMJ tissue engineering. Hollister and colleagues[20] implanted a 3D printed mandibular condyle scaffold coated with bone morphogenetic protein (BMP)-2 into the temporalis muscle of Yucatan mini-pigs. After cellular infiltration and vascularization were established, a horizontal condylectomy was performed and the scaffold was fixed in place. After 6 months, computed tomography (CT) scans and histology suggested vascularization, bone infiltration, and signs of neocartilage formation in the porous condyle scaffold. Chen et al.[14] pre-cultured autologous stem cells on subject-specific decellularized bone matrix geometries for 6 weeks before implantation.

The bioreactor-derived cartilage-bone construct regenerated tissues that more closely resembled control cartilage and subchondral bone tissues than either bone-only or acellular grafts. Previously, our group employed an acellular approach with a gradient of growth factors in a cylindrical, microsphere-based scaffold to regenerate focal mandibular condyle defects in rabbits.[21] Research to date has reported signs of mandibular condyle bone and cartilage regeneration with a seeded scaffold approach,[22] yet a practical approach that can be rapidly produced for off-the-shelf immediate implantation for successful regeneration of continuous bone and cartilage tissues remains elusive.

A resorbable scaffold that can support loads and regenerate mature, stratified cartilage on the articulating surface of regenerated bone leaving no trace of the implanted material remains a common limitation for TMJ tissue engineering.[14,18,23] Significant bone regeneration has been documented with porous polycaprolactone (PCL) and hydroxyapatite (HAp) scaffolds.[24] In this study, a biphasic scaffold prosthesis was assembled from two parts: (1) an anatomically correct 3D printed bone regeneration structure comprising porous polycaprolactone and 20% w/w hydroxyapatite (PCL-HAp) and (2) a potentially chondrogenic hydrogel comprising photocrosslinkable, 4% w/v pentenoate-modified hyaluronic acid (PHA), 20% w/v polyethylene glycol (PEGDA), and 15% w/v devitalized cartilage (DVC).[25–27]

Chondrogenesis and mechanical properties of the PHA-PEGDA-DVC hydrogel were previously reported by our group.[28] The 3D printed PCL-HAp was characterized for structure, mechanical properties, and biofluid transport. A Spanish cross goat model with an approximately human-sized TMJ was used to evaluate tissue regeneration in a pilot study over 6 months of orthotopic implantation.[15] PCL-HAp only, and a biphasic PCL-HAp + PHA-PEGDA-DVC hydrogel-integrated condylar prosthesis were evaluated against native tissues from the contralateral condyle. The purpose of the study was to characterize an acellular scaffold and regenerate bone throughout the condylar head with cartilage regeneration on the condyle's articulating surface.

Methods

Three-dimensional printing biphasic prosthesis and cartilage-matrix hydrogel synthesis

Polycaprolactone (PCL, 50 kDa; Polysciences, Inc., Warrington, PA) filament with 20% w/w hydroxyapatite powder (HAp; Sigma-Aldrich, St. Louis, MO) was made using a filament extruder (Noztek Touch, Shoreham, West Sussex, or Filabot Ex6, Barre, VT). PCL and HAp were mixed with the desired ratio and planetary ball-milled for 6 h (PQ,N2 Across International, Livingston, NJ), and extruded at 135°C at a rate of 30 rpm. Filament was fed into a Flashforge Creator Pro printer (Zhejiang, P.R. China) for 3D printing at 135°C.

For 3-point bend testing, parts were printed on a Cura Lulzbot Taz 6 3D printer (Lulzbot, Fargo, ND) with the same parameter settings as the Flashforge. A patient-fitted prosthesis was digitally designed using CT scans of each goat (16-slice Philips CT, Amsterdam, Netherlands) with a microporous architecture inside the condylar head (Fig. 1A). Three-dimensional printed PCL-HAp was then submersed in 5 M NaOH for 30 min, washed 3× in DI water, and sterilized overnight using ethylene oxide. Two different prosthesis groups were made either without a hydrogel (i.e., PCL-HAp only), or with PHA-PEGDA-DVC hydrogel syringed onto the surface and into mechanical integration features.

The hydrogel was synthesized as previously described.[28] Briefly, 1.5 MDa hyaluronic acid (HA; Lifecore Biomedical, Chaska, MN) was dissolved and functionalized with 4-dimethylamino pyridine and 4-pentenoic anhydride added at 0.25 g per g HA and 10-fold molar excess, respectively (Sigma-Aldrich). Functionalized PHA solution was

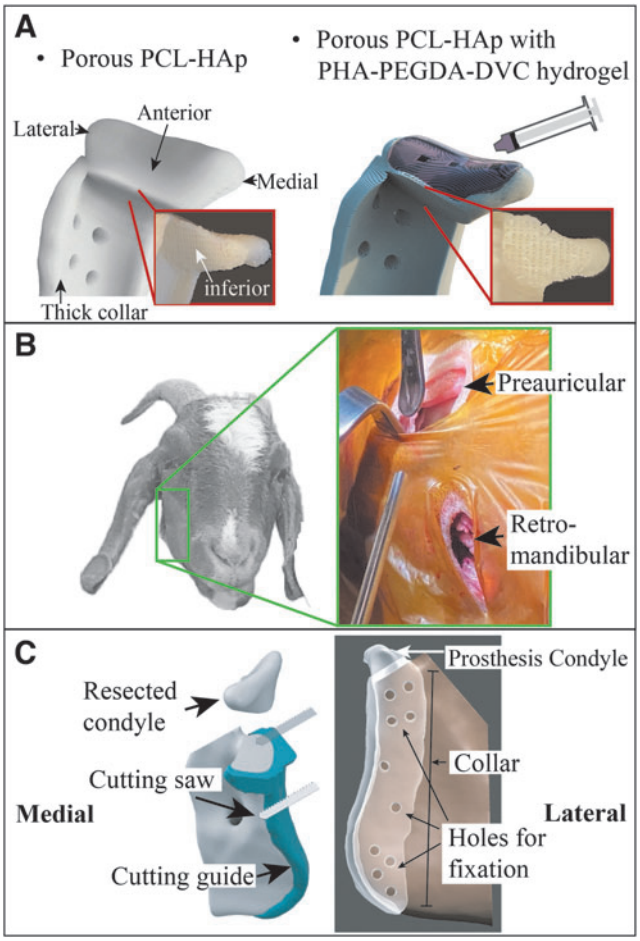

FIG. 1. Schematic diagram of the prosthesis and surgical implantation. **(A)** Two prosthesis designs were orthotopically implanted: (1) A smooth PCL-HAp prosthesis, and (2) a biphasic prosthesis with both PCL-HAp and a chondrogenic hydrogel comprised of PHA, PEGDA, and DVC was syringed onto the interlocking condyle with a recessed surface and UV crosslinked such that the integrated hydrogel was flush with the condyle surface. Both prosthesis designs had a porous internal architecture. **(B)** Surgical implantation was performed with preauricular and retromandibular incisions. The condyle was resected through the preauricular incision, and then the prosthesis was inserted through the retromandibular incision. **(C)** To resect the condyle, a cutting guide was inserted and fixed to the mandible. Subsequently, the guide was removed, and the prosthesis was inserted and fixed into position. DVC, devitalized cartilage; PCL-Hap, polycaprolactone-hydroxyapatite; PHA, pentenoate-modified hyaluronic acid; PEGDA, polyethylene glycol.

precipitated using acetone, purified, and frozen, before lyophilization on a FreeZone 6 Plus lyophilizer (Labconco, Kansas City, MO) and stored at −20°C.

NMR characterization of PHA was performed as previously described[29] with a 64% functionalization of the disaccharide repeat units.

Porcine knees (Hampshire and Berkshire, female, 1-year old, 180–220 kg) were obtained from a local abattoir to prepare DVC powder from cartilage as previously described.[26] The DVC was lyophilized and stored at −20°C.

Hydrogels were prepared with 4% PHA, 20% PEGDA, and 15% w/v DVC as previously described.[28] The photoinitiator, 2.2 mM lithium phenyl-2,4,6-trimethylbenzoylphosphinate (LAP; 98%; TCL0290-1G) (TCI America, Portland, OR), was prepared in phosphate-buffered saline (PBS; Sigma-Aldrich). Once dissolved, the crosslinker dithiothreitol (Sigma-Aldrich) was added to ensure a 1:1 thiol:ene molar ratio for all composites. Precursor mixtures were spatulated for at least 15 min and then syringed onto the 3D printed scaffold bedside before photocrosslinking for 10 min (365 nm light at 1280 $\mu W \cdot cm^{-2}$, EA-160; Spectroline, Westbury, NY).

CT scans from each goat were registered and implants designed following consultation with TMJ concepts. Each scan was segmented for the condyle and ramus using Seg3D (University of Utah SCI Institute). The part was enlarged such that a 0.165 mm offset resulted between prosthesis and bone. A condyle cutting plane was derived from points in the superior external auditory meatus and inferior orbit. The implant collar was extruded from the ramus surface and combined with the resected condyle in Meshmixer (San Rafael, CA). All screw holes were 0.094.''

Surgical implantation

All experiments were performed with the approval of the Institutional Animal Care and Use Committee. After a surgical plane of anesthesia was achieved (Supplementary Data S1), two incisions were performed to gain access to the bone, and permit both the guided condylectomy and the condylar implants insertion (Fig. 1B). Initially, a preauricular incision was performed 1 cm below the zygomatic arch, parallel to the posterior border of the mandible with ~2.5 cm of extension. After that, another 2.5 cm long retromandibular incision was performed in a curvilinear manner, following the mandibular angle contour at the level of the mandibular inferior border. The two incisions were separated by a length of ~2 cm.

After reaching the bone, subperiosteal dissection was accomplished to expose the medial and the lateral aspects of the ramus and condyle, with attention to preserve the disc. After adequate level of dissection was obtained, a custom-made cutting guide was inserted through the retromandibular incision and fixed to the ramus with four titanium screws (KLS Martin, Jacksonville, FL), thus providing a planar guide for condyle resection, performed using a Bien-air reciprocating saw (Bien-air Dental, Bienne, Switzerland). The condyle was then disinserted and removed, taking care to preserve the disc, and the cutting guide was replaced by the implant, which was fixed in place with eight screws (Fig. 1C).

Load transmission to underlying jaw

To estimate physical forces transmitted to the underlying bone, a uniaxial mechanical testing setup was used to evaluate loads in two locations: (1) applied to the surface of the condyle, $F_{Applied}$, and (2) $F_{Transmitted}$ measured between the prosthesis condyle and underlying jaw structure with a FlexiForce pressure sensor (Barneveld, Netherlands) (Fig. 2). The % load transmitted was calculated using the following equation.

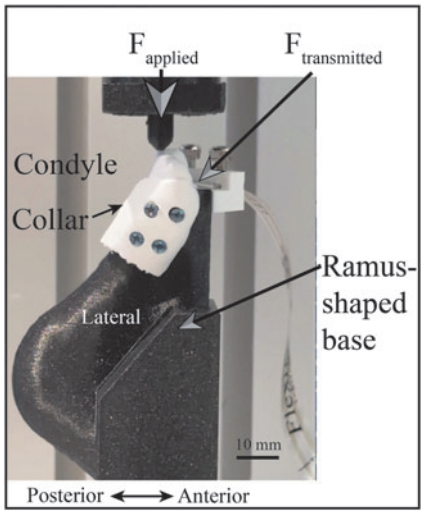

FIG. 2. Illustration of the testing setup for load transmission. The upper half of the prosthesis was fixed to a 3D printed ramus-shaped base. A 5 lb_f load was applied to the condyle and the transmitted load was measured with a force-sensitive resistor positioned between the condyle and the base. Following each sample, the force sensitive resistor was calibrated by repeating the test with an unconstrained condyle.

$$\%\ Load_{transmitted} = \frac{F_{Transmitted}}{F_{Applied}} \cdot 100\% \quad (1)$$

Experiment

Animals

Six Spanish cross female goats (initial weight: 33 ± 5 kg, final weight: 52 ± 13 kg, and age: 3–5 years) were used in this study. All goats were purchased and boarded at the University of Oklahoma Health Sciences Center Division of Comparative Medicine. Goats were assigned to two pilot groups for 6-month implantation periods with either no-hydrogel or a hydrogel-integrated prosthesis.

Structural characterization of 3D printed prosthesis

Three dimensional printed PCL-HAp specimens were sputter coated with gold on a Hummer VI (Anatech Ltd., Battlecreek, MI), and examined under a field emission scanning electron microscope (SEM; Zeiss NEON 40 EsB, Stuttgart, Germany) with 5 kV acceleration voltage. Furthermore, energy-dispersive X-ray spectroscopy (EDS) was used to identify elemental structure.

Uniaxial tensile testing

Uniaxial testing followed American Society for Testing and Materials (ASTM) standard #D1708. Briefly, dog bone shapes with a 5×3 mm cross-section, and 22 mm gauge length were extended uniaxially at a rate of 1 mm $\cdot$ min^{-1} in a TestResources uniaxial tester (Shakopee, MN). Three groups were evaluated for tensile properties: (1) PCL, (2) PCL-HAp, and (3) etched PCL (ePCL-HAp). For ePCL-HAp, the composite was submersed in 5 M sodium hydroxide (30 min) to improve hydrophilicity and washed thrice in DI water before testing. Linear regression from 5% to 30% of the ultimate strain was used to obtain the Young's modulus. The ultimate stress and strain were determined from the global maximum stress, and the yield stress and strain were determined using the 0.2% strain offset. $n = 5$–6.

Three-point bend testing

PCL, PCL-HAp, and PCL-HAp beams were 3D printed ($70 \times 15 \times 3$ mm) and tested for flexural stiffness following ASTM standard #D790. A span length of 48 mm was set on a 3-point bending fitting for the TestResources machine. Beams were deflected at a flexural strain rate of 1% $\cdot$ min^{-1} to 5% flexural strain. The flexural modulus was determined from the slope of the 1–2.5% flexural strain range. Beams were printed on the Cura TAZ 6 Lulzbot 3D printer. $n = 6$.

Load transmission test

PCL-HAp prostheses with either a thick, 5 mm collar used in the current animal study, or a thin, 3 mm collar prosthesis were tested for load transmission. Prosthesis fixation was achieved using the top four screw points where only the top half of the prosthesis with the condyle was printed and tested. A load was applied at a rate of 10 lb $\cdot$ min^{-1} to 5 lbs. and held for 1 min. Transmitted load was measured on a FlexiForce load sensor (Tekscan, Norwood, MA), preconditioned with a 70 lb_f load for 5 min. After each data-collection run, a calibration run was performed with an unconstrained condyle. A power law equation was fit to the calibration data to convert signal to transmitted load from the FlexiForce sensor. $n = 4$.

Biofluid transport through capillary rise

Scaffolds from either PCL-HAp or ePCL-HAp were printed to assess whole blood capillary rise through the porous architecture. A $10 \times 10 \times 3$ mm scaffold was printed with a zig-zag pattern and 0.60, 0.85, and 1.10 mm line distances such that the actual cross-sectional pore sizes were 152 ± 68, 360 ± 140, and 570 ± 240 μm for the 150, 350, and 550 μm groups, respectively. A bath with whole goat blood (Innovative research, Novi, MI) was raised to contact the scaffold. Imaging was captured at 60 fps and a custom MATLAB script was used to process each image and calculate an ensemble average of the blood height. The initial velocity for each sample was calculated from a linear fit to the initial 2s of data. $n = 6$–7.

Bone assessment with Micro-CT

At the 6-month completion of the study, each implant was resected *en bloc* along with the TMJ disc and fossa. The specimens were then scanned with a micro-CT system set to 70 kV, and 200 μA (Quantum FX, Perkin Elmer Co, Waltham, MA) with a 30 mm field of view. Each scan was segmented using Seg3D (University of Utah SCI Institute) for implant, screw, and bone materials. A custom MATLAB script was used to register each object in space for consistent viewing perspectives. Renderings of the segmented and registered objects were performed using Autodesk Fusion 360 (San Francisco, CA).

Soft tissue assessment with histology and immunohistochemistry

Resected tissue specimens were fixed in 10% neutral buffered formalin (VWR, Radnor, PA), dissected, and imaged for gross morphology. Boney tissues were decalcified in newcomer supply (Newcomer Supply, Fisher, Hampton, NH) for at least 4 months before sectioning with a blade. All tissues were dehydrated in 70% ethanol (VWR) overnight and paraffin embedded for slide mounting. Slices 4-μm thick were mounted and stained with hematoxylin and eosin (H&E), or Alcian blue on a ST5020 workstation (Leica, Wetzlar, Germany).

Immunostaining was performed with a Leica BOND III BOND RX automatic system with a 12-h antigen-retrieval step at 60°C at pH 9.0 to prevent bone delamination. Soft tissue specimen antigen retrieval was performed at 100°C for 20 min at pH 6.0. For collagen II and CD4 immunostaining, rabbit primary antibodies were purchased from Abcam (#ab34712, Cambridge, United Kingdom) and Novus (#NBP1-19371SS, St Louis, MO), respectively. For secondary antibody, post-primary IgG-linker reagent was used with 3,3′-diaminobenzidine tetrahydrochloride (DAB) as chromogen and counterstained with hematoxylin. Antibody-specific positive and negative control (omission of primary antibody) were parallel stained. Additional positive control tissue for CD4 was obtained from goat submandibular lymph node.

TMJ disc gross morphology scoring

TMJ discs were randomly sorted and scored by four oral surgery clinicians. A scoring system was modified from van den Borne et al.[30] with a range from 0 (poor) to 4 (excellent).

Statistical analyses

Statistical analyses were performed with one-way ANOVA with Tukey's *post hoc* test, or a one-way *t*-test for two groups. Significance was defined when $\alpha = 0.05$. All data were mean ± standard deviation.

Experimental Results

Animals

Five goats were euthanized after 6 months and one euthanized early (4 months) due to conditions unrelated to the study, that is, a caseous lymphadenitis caused by a *Corynebacterium pseudotuberculosis* infection likely contracted before boarding (Supplementary Data S1). Results were thus reported for three no-hydrogel and two hydrogel group specimens. All animals exhibited weight gain averaging 18 ± 10 lbs. over the study duration and resumed normal jaw function within 2 h of surgery.

Structural and mechanical properties of 3D printed prosthesis

EDS exhibited a homogeneous distribution of calcium and phosphorous throughout 3D printed PCL-HAp (Fig. 3).

Young's moduli increased by 67% with the addition of HAp relative to PCL PCL-Hap, with no difference after etching (Fig. 4C). Strain energies were 1.8-fold higher in PCL than PCL-HAp, and not different between PCL-HAp and ePCL-HAp (Fig. 4D). Ultimate tensile stresses and yield stresses did not exhibit differences among groups (Fig. 4E, G). Ultimate strains reduced by 0.6-fold from PCL to PCL-HAp, and ePCL-HAp (Fig. 4F). Furthermore, yield strains were 1.5-fold higher in PCL than in PCL-HAp and ePCL-HAp (Fig. 4H).

Flexural stiffness was 2.06-fold higher in PCL-HAp than the PCL group, but did not change after etching (Fig. 5).

Load transmission to underlying bone grip was ~12% higher for thin-collared implants than for thick-collared implants, which were used in this study's pilot animal study (Fig. 6).

Porous architecture supports whole blood infiltration

For all the NaOH-etched scaffolds, capillary rise of whole blood reached the full 1-cm height within 1 min (Fig. 7A). Small, 152 ± 68 μm pore length scaffolds exhibited an initial velocity of $3.7 \pm 1.2\ \text{mm} \cdot \text{s}^{-1}$, and increasing pore sizes reduced the initial velocities by 31% and 77% for 360 ± 140 and 570 ± 240 μm, respectively (Fig. 7B). Differences in initial

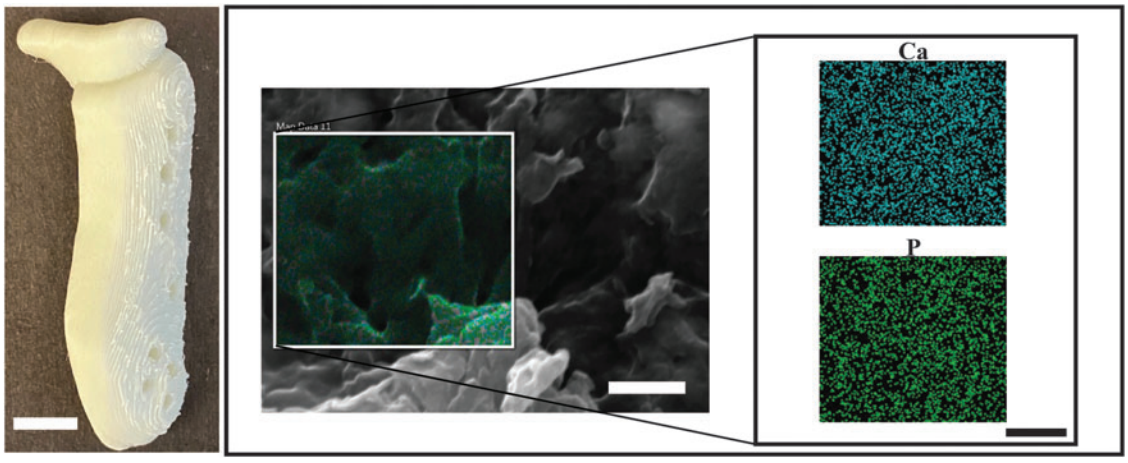

FIG. 3. Calcium and phosphorous were distributed throughout the 3D printed PCL-HAp. Scanning electron microscopy (SEM) of 3D printed PCL-HAp using energy-dispersive x-ray spectroscopy exhibited homogeneously distributed calcium and phosphorous. Scale bar for left-hand image of prosthesis was 10 mm. Scale bars for SEM and EDS were 1 μm. EDS, energy-dispersive X-ray spectroscopy; Ca, calcium; P, phosphorus.

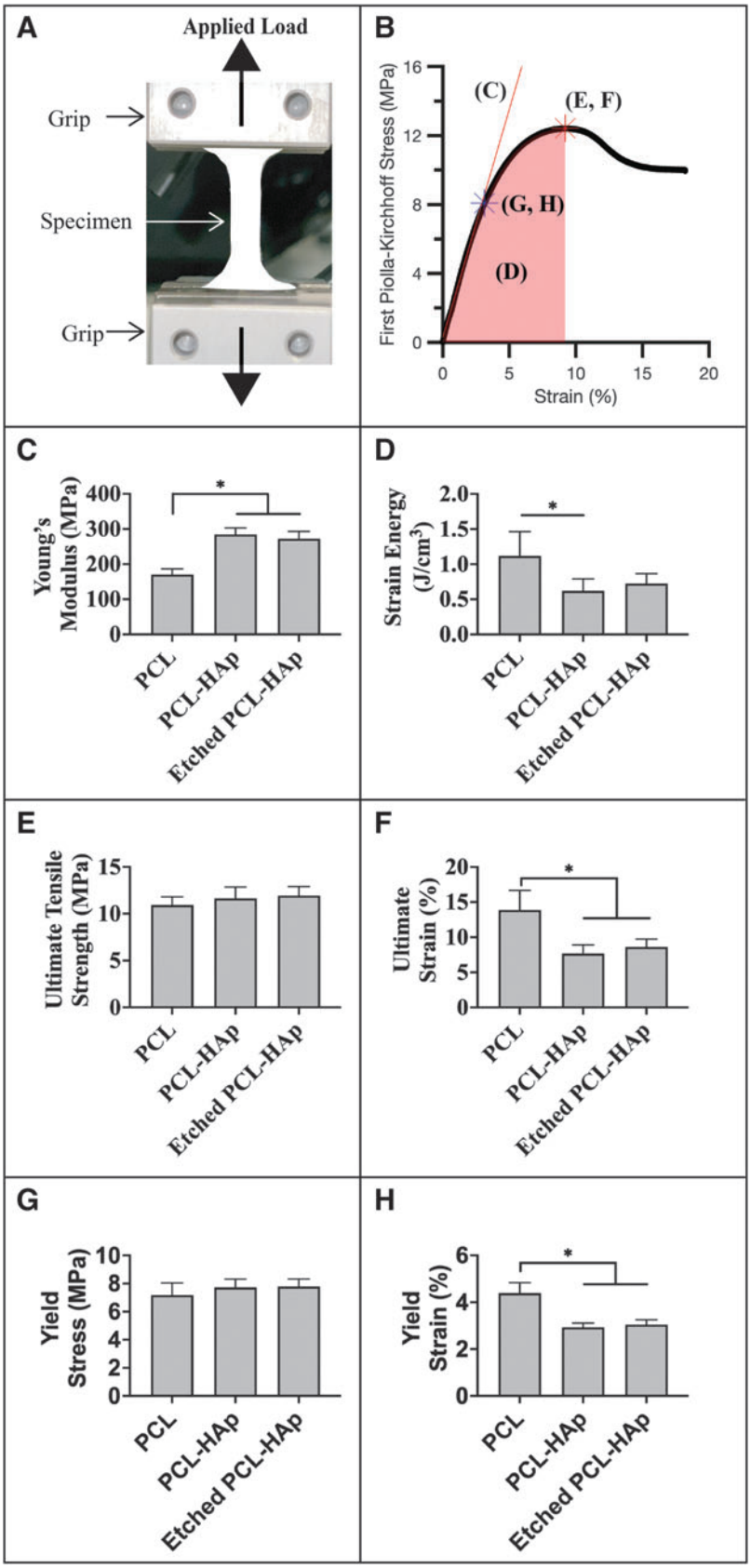

FIG. 4. Uniaxial tension of 3D printed PCL-HAp. Adding HAp significantly enhanced PCL's mechanical performance. **(A)** Illustration of test following ASTM D1708. **(B)** Representative stress/strain plot where *letters* C–H refer to the parameters reported in the following panels. **(C)** The addition of HAp significantly enhanced PCL stiffness, but not after NaOH etching compared to nonetched PCL-HAp. **(D)** Strain energy decreased with the addition of HAp, but not after NaOH etching compared to nonetched PCL-HAp. **(E)** The ultimate tensile strengths did not differ among groups. **(F)** Ultimate strains decreased with the addition of HAp, but not after NaOH etching compared to nonetched PCL-HAp. **(G)** Similar yield stresses were exhibited across the different groups. **(H)** The yield strain decreased with the addition of HAp to PCL, but not after NaOH etching compared to nonetched PCL-HAp. $n = 5–6$. $^*p < 0.05$. All data are mean ± standard deviation. HAp was 20% wt.

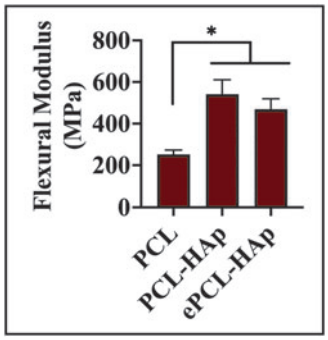

FIG. 5. Three-point bend test of 3D printed composites following ASTM D790. The addition of HAp increased PCL flexural stiffness, but the reduction in stiffness after NaOH etching (ePCL-HAp) was not different from nonetched PCL-HAp. $n = 6–7$. $*p < 0.05$. All data are mean ± standard deviation. HAp was 20 wt%.

velocity were not exhibited by the etched 150 and 350 μm groups. Nonetched scaffolds exhibited negligible capillary rise (Fig. 7B).

Bone growth and resorption surrounding condyle

Bone growth and resorption exhibited by micro-CT-derived renderings were highly variable from specimen to specimen. Resorption was focused to regions directly under the prosthesis condyle and a gap was left between the prosthesis collar and bone (Fig. 8). An approximate measurement made on MicroCT images suggested the depth of resorption was lower in the no-hydrogel group (A: 6.0, B: 5.6, and C: 2.6 mm) than the hydrogel group with lengths of D: 7.2 and E: 9.2 mm. Bone growth surrounding the implanted condyle was localized to both the medial and posterior regions of the condyle. In all cases, except B, soft tissues enveloped the condyle.

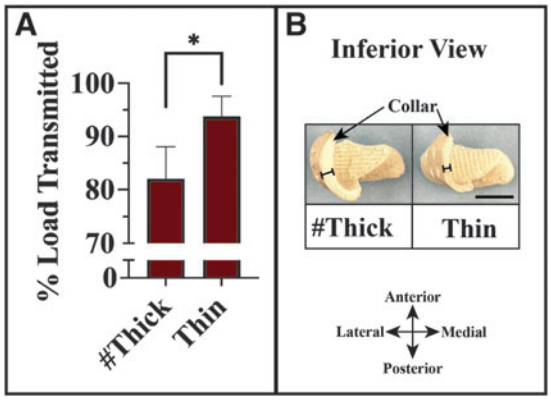

FIG. 6. Evaluation of the load transmitted through the condyle to the underlying bone geometry. **(A)** As the collar region of the prosthesis was reduced in thickness from ~5 mm (thick) to 3 mm (thin), the transmitted load increased by over 10%. **(B)** Thick and thin collar prostheses. %Load transmitted = $F_{transmitted}/F_{applied}$ * 100%. #Thick specimen was the design parameter selected for the prostheses implanted in the pilot animal study. The pilot study used full-length prostheses that extended to the angle of the mandible. Scale bar: 10 mm. $*p < 0.05$. $n = 4$. Data are mean ± standard deviation.

Possible neocartilage in regenerated soft tissue

Sagittal sections of soft tissue enclosing the implanted condyle exhibited signs of neocartilage formation. Positive Alcian blue and collagen II staining were localized to the functional anterior side in nonhydrogel C and hydrogel-integrated D implant (Fig. 9). CD4 staining for helper T cells was variable with faint to no stain in the control, B, C, and D to moderate staining in A and E.

TMJ disc histology

Histology of the TMJ discs exhibited highly variable results from perforated, granulation tissue, to nearly pristine (Fig. 10). No observable granulation tissue was exhibited by the discs for control, B, C, and E. For B, a central disc perforation was observed. Discs for A and E presented with granulation tissue. For C, the disc histology closely matched that of the unoperated control disc.

TMJ disc gross morphological scoring

Disc scores suggested degeneration, hypertrophy, and irregular macroscopic appearances for discs A, B, and E (Table 1). Although goat B scored 0 for degeneration due to perforation, the macroscopic appearance scored 1.8, higher than discs A (1.3) and E (1.0). Discs A and B scored 30% higher overall than goat E. The disc from goat C scored slightly higher than the average control disc score (4.0 vs. 3.9). It is noteworthy that the disc from goat C appeared longer anteroposteriorly and shorter mediolaterally than the contralateral control disc. No score could be collected for goat D because the disc fused to the condyle, making it difficult to discern disc tissue from other soft tissues.

Discussion

This study demonstrated the feasibility of an acellular, biphasic TMJ prosthesis for immediate loading. The integrated hydrogel prosthesis exhibited variations in gross appearance and staining of key neocartilage markers. Specifically, one specimen from each group (hydrogel and no-hydrogel) exhibited collagen II and Alcian blue staining. CD4 staining was pronounced in one specimen from each group, and the remaining specimens exhibited little CD4 staining. It is possible that higher inflammation was associated with CD4 staining, although Vapniarsky et al.[31] demonstrated animals with chronic inflammation did not exhibit higher levels of CD4 compared to a negative control. All specimens featured fibrous soft tissues throughout the condylar head's porous architecture. Furthermore, the TMJ disc exhibited variable gross appearances and Alcian blue staining, with a nearly pristine disc coming from a hydrogel-free prosthesis.

Further studies may examine strategies for TMJ disc management and attachment during implantation. In addition, a more sophisticated, zonal material approach may be warranted to integrate stratified subchondral bone, and layered cartilage structures into a regenerated mandibular condyle. Adjustments to both biochemical (e.g., BMP-2) and physical (e.g., adjusting pore size, loading to bone, and degradation) signaling could be incorporated into the prosthesis design to improve tissue regeneration and reproducibility.

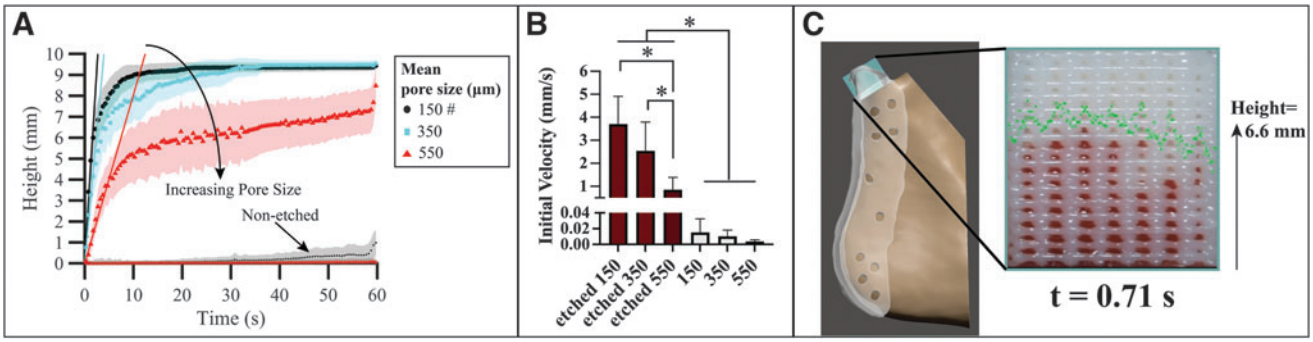

FIG. 7. Three-dimensional printed PCL-HAp composite scaffold exhibited capillary rise of whole blood. **(A)** The rates decreased as pore sizes increased (150, 350, and 550 μm). Negligible capillary rise was exhibited by scaffolds that were not etched (*green plot* with *arrow*). A line was fit to the initial data points to calculate each group's initial velocities. **(B)** The etched group initial velocities decreased by 31% and 77% for 350 and 550 μm groups from $3.7 \pm 1.2\,\text{mm}\cdot\text{s}^{-1}$ for the 150 μm group. Negligible capillary rise was detected in the nonetched groups (*gray bars*). Differences were exhibited among all groups, except within nonetched groups (*gray bars*) and the etched 150 and 350 groups. **(C)** The prosthesis was designed with a 150 μm porous structure inside the condylar head. Representative specimen illustrated digital measurement of whole blood height (*green* ''Xs''). #Denotes 150 μm pore size used in the animal study. Data points are ensemble averages, bands are standard deviations. $p < 0.05$. $n = 7$.

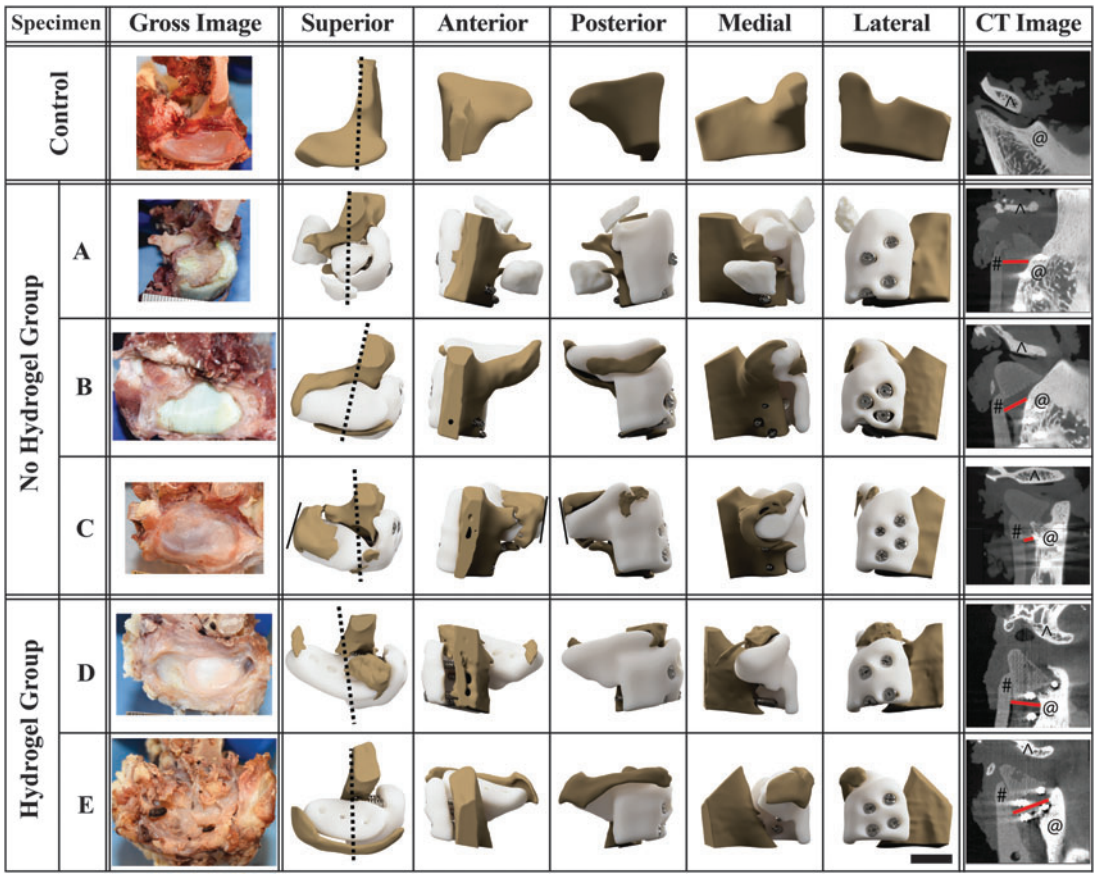

FIG. 8. Assessment of bone with MicroCT data prepared from each subject 6 months after implantation. Gross images were captured from the tissue's superior viewpoint with the camera pointed from the superior perspective. Renderings for each case were displayed with the view direction listed across the *top row* (superior, anterior, posterior, medial, and lateral). In each case, bone growth was exhibited around the prosthesis condyle, but not inside the condyle's porous region. Bone resorption was observed in all cases with more pronounced bone loss in groups with the hydrogel (D, and E). The control group is shown as the mirror image of the *left* condyle from subject C to facilitate visual comparison with the experimental group *right* condyles. In the CT images, the prosthesis, ramus bone, and fossa bone were labeled as #, @, and ^, respectively. The prosthesis was displayed as white, and bone as brown in the renderings. Dashed line in 'superior' column represents plane of CT image in right-most column. The approximate distance between the prosthesis collar and bone was shown with a *red line* superimposed on the CT sections. The approximate lengths were 6.0, 5.6, and 2.6 mm for nonhydrogel groups A, B, and C, and 7.2, 9.2 mm for groups D and E, respectively. MicroCT imaging volume was focused on the condylar region, although the prostheses extended down to the angle of the mandible. Scale bar: 10 mm.

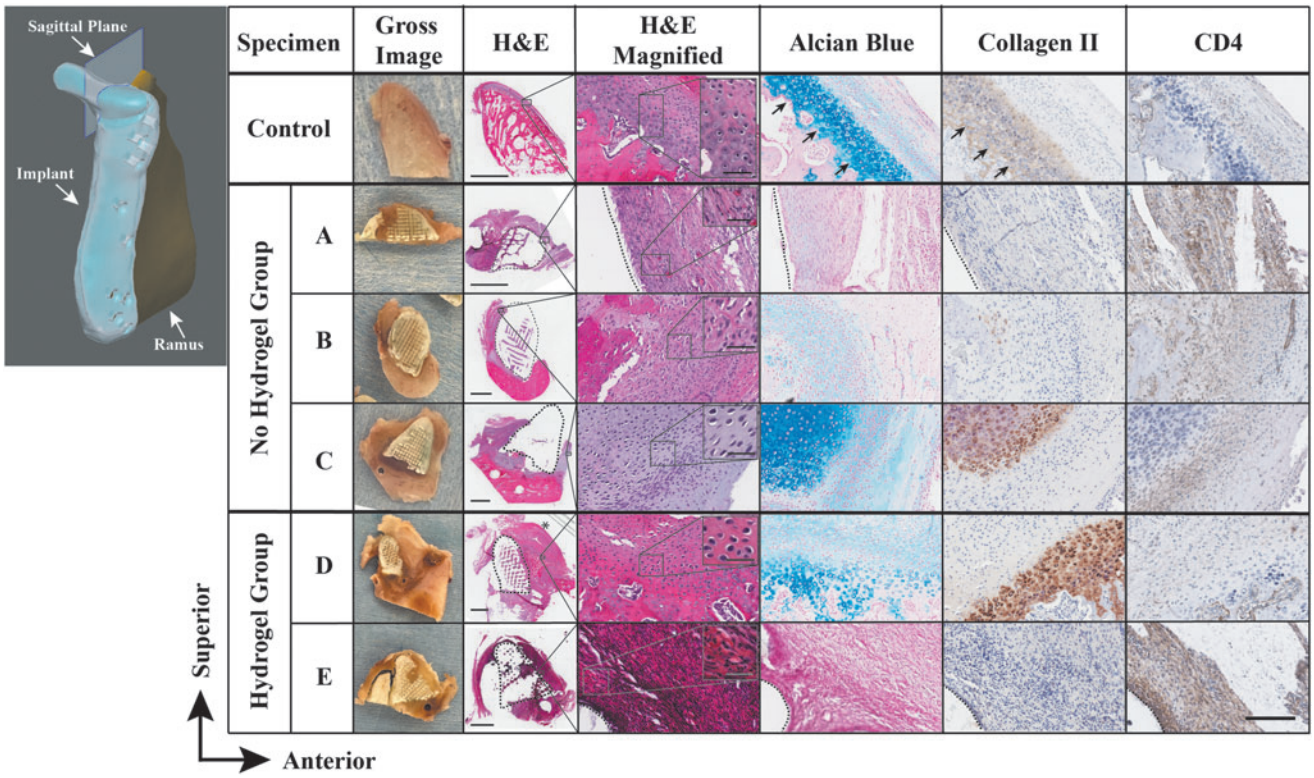

FIG. 9. Assessment of neocartilage and bone formation with histology and immunohistochemistry from selected regions of sagittal condyle sections. Note in the healthy control tissue the deeper hyaline-like cartilage layer (*black arrows*) below the overlying proliferative and superior fibrous zones. Cases C (without hydrogel) and D (with hydrogel) exhibited evidence of cartilage-like soft tissue regeneration. Alcian *blue* staining was exhibited by the control mandibular condylar cartilage's deep layer, and in subjects A, B, C, and D with the richest experimental tissue staining in C and D. Collagen II staining was exhibited by the control specimen's deep layer, in addition to subjects C and D on the anterior, articulating surfaces. Subject B exhibited faint collagen II staining in the pericellular matrix. Generally, high collagen II staining was localized to the pericellular matrix. Specimens A and E exhibited darker CD4 staining for helper T cells than the other cases, suggesting a variable innate immune response. Little to no CD4 staining was exhibited by the contralateral control condyle. The disc fused to the surface of condyle D shown with *. Gross images presented the tissue sections before slide mounting. Illustration of ramus and condylar prosthesis (*left panel*) with sagittal plane was provided for orientation purposes. *Dashed lines* represent prosthesis border. Scale bars: 3 mm for H&E, 50 μm for *insets*, and 200 μm (*lower right*) for all other images. H&E, hematoxylin and eosin.

In both hydrogel and no-hydrogel groups, the prosthesis restored chewing function in a human-sized TMJ model. All subjects resumed eating a normal diet and gained weight throughout the study period. Bone responses to the scaffolds, however, were variable with regions of resorption immediately under the prosthesis. The condyles in some cases appeared to have plastically deformed toward the underlying ramus. Tensile testing revealed that the Young's modulus of PCL was enhanced to 269 MPa by the addition of HAp. For comparison, the compressive modulus of PCL-HAp has been reported in the range of 20 kPa to 150 MPa.[32–34] Additional bending support in the collar of the prosthesis was enhanced by the HAp with a flexural modulus of 470 MPa.[35–37] For plastic deformation or failure, strains beyond 3% in the prosthesis collar were likely allowed by resorption of supporting bone.

There are many different sources of signaling for bone maintenance and growth, including mechanical forces to the underlying bone. The mechanical loading regimen most suitable to restore bone remains unclear for the TMJ. Loads of $\sim$20 lb_f have been measured in Macau condyles, and loads of 5 lb_f were estimated from a study with humans during normal chewing function.[38,39] Analysis of joint implants has suggested higher load transmission can prevent stress-shielding and thus improve bone density.[40,41] In contrast, dental implants may fail to osseointegrate when immediately loaded without a 4–6-month period of load-free conditions.[42,43] In this study, we introduced a method with a load sensor to measure transmitted loads.

The prosthesis design in this study transmitted a significant proportion of a 5 lb_f applied load (>80%) to the supporting structure, and yet all subjects exhibited bone loss. In contrast, high stiffness metal TMJ implants rarely exhibited significant bone loss with reports of functional success for over 20 years.[44,45] A more refined understanding of the types and magnitudes of stresses that encourage bone formation may be important to successful bone regeneration strategies in immediate TMJ loading applications.[38,46–48] The load transmission test introduced in this study may be useful in future work for TMJ prosthesis

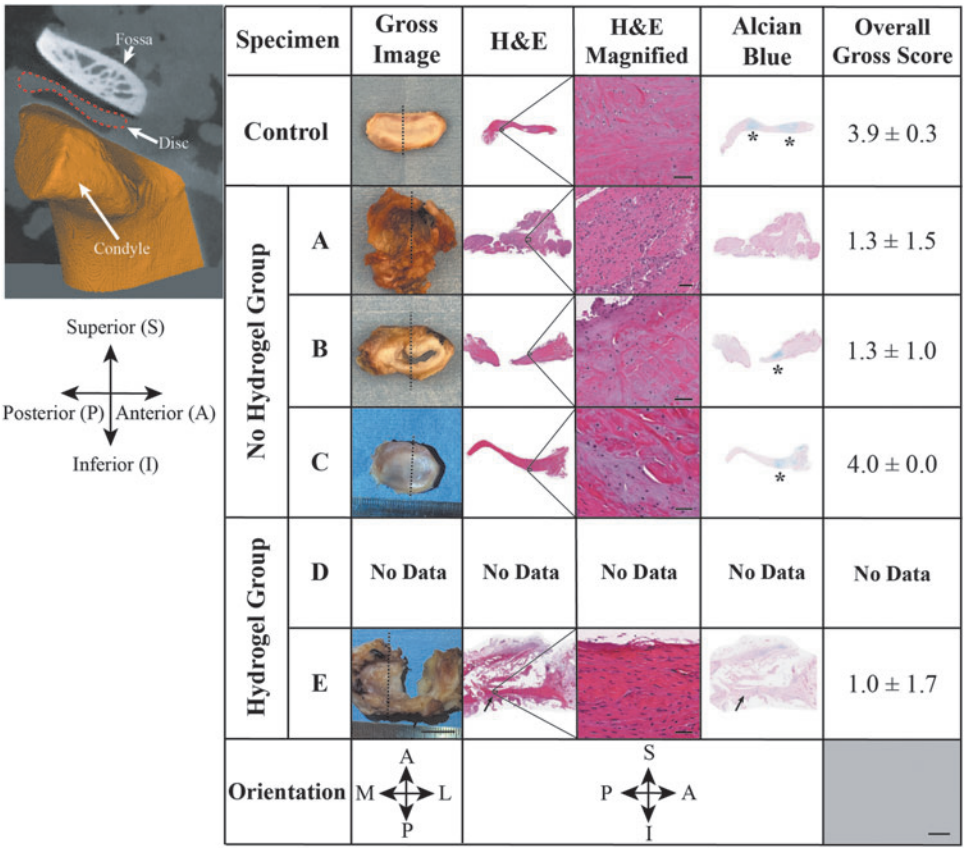

FIG. 10. Assessment of TMJ disc structure with histology. Disc outcomes were variable from nearly pristine to perforated. MicroCT after tissue resection illustrates approximate disc location relative to condyle and fossa. Gross images exhibit changing sizes among disc tissues. Subjects A and E exhibited granulation tissue, with some remaining discernable disc tissue in subject E (*arrow*). Subject C disc tissues matched the histological structure of the control, although the aspect ratio appears to have changed to a shorter medial-lateral and longer anterior-posterior than control disc. In subject D, the disc fused to the condyle; hence, there were no data. Alcian blue staining was positive in a distinct band in the control disc (*). Alcian blue staining persisted in B and C, although was largely absent in A and E. The overall gross morphology score was highest in subject C. Details regarding scoring information can be found in Supplementary Table. Orientations were medial (M), lateral (L), anterior (A), and posterior (P) for the gross images; and superior (S), and inferior (I) for histology images. Control displayed as mirror image for comparison with experimental data contralateral side of jaw. *Dashed lines* denote sectioning. H&E staining. Scale bars are 10 mm for gross images, 50 μm for H&E magnified *column*, and 3 mm for remaining images (*lower right*). TMJ, temporomandibular joint.

designs that take bone mechanotransduction into consideration. Clinical joint immobilization following surgical implantation may be a further consideration for bone integration.[49]

Neocartilage formation suggested evidence of a functional environment for cartilage tissue stimulus. Staining for Alcian blue and collagen II was localized to the anterior, functioning surface of a prosthesis that had no hydrogel to provide any chondroinductive cue. The posterior, nonfunctioning surface of the condyle exhibited no Alcian blue or collagen II staining. Furthermore, for the integrated hydrogel case, there were signs of bone formation on the anterior surface, although positive Alcian blue and collagen II were exhibited in a region adjacent to new bone on the anterior surface. These observations

Table 1. Gross Morphology Grading Scale for Temporomandibular Joint Disc Evaluation

Group	*Specimen*	*Degeneration*	*Hypertrophy*	*Macroscopic Appearance*	*Overall*
Control		3.8 ± 0.6	4.0 ± 0.0	4.0 ± 0.0	3.9 ± 0.3
No Hydrogel	A	1.3 ± 1.5	1.3 ± 1.5	1.3 ± 1.5	1.3 ± 1.5
	B	0.0 ± 0.0	1.0 ± 0.8	1.8 ± 1.5	1.3 ± 1.0
	C	4.0 ± 0.0	4.0 ± 0.0	4.0 ± 0.0	4.0 ± 0.0
Hydrogel	D	No Data	No Data	No Data	No Data
	E	0.8 ± 1.5	0.5 ± 0.6	1.0 ± 1.4	1.0 ± 1.7

were in agreement with the concept of using functional loading to regenerate cartilage tissues.[50,51]

Although it may not be possible to determine cell source for regenerated neocartilage based on staining and morphology from histology, potential tissue sources that could contain progenitor cells were considered based on anatomic proximity. Given the higher numbers of stem cells in bone marrow than blood, adipose, or TMJ, the cell source for regenerated condylar tissues could likely have been bone marrow from the ramus or through systemic circulation.[52] The TMJ disc is a dense collagenous structure, but evidence of vasculature through the TMJ disc could provide transport for some *Chad*+ chondrogenic fibroblasts.[53,54] Future work may be able to develop cell lineage tracking methods to provide compelling evidence for the origins of regenerated tissue.[14,55–57]

Within the condyle porous architecture, highly aligned fibrous tissues formed, although more time *in vivo* could potentially allow for mineralized tissue formation. This study emphasized a capillary rise scaffold design with $\sim 150\,\mu m$ pore sizes to gain regenerative utility from the native cells located in the adjacent ramus bone marrow. Future work may explore larger, transport-sustaining pore sizes, or other pore geometries to better stimulate osteogenesis throughout the scaffold.[58,59]

The health of the TMJ disc offered signs of functional joint regeneration. Pristine disc structures scored higher than the average control disc throughout the 6-month implantation period. The presence of Alcian blue staining in the disc, although only on the anterior region, suggested a healthy disc structure. However, other cases here exhibited disc perforation, or granulation tissue, and potential signs of fibrous ankylosis with disc fusion to the condyle. Tissue-scale pathogenesis of ankylosis in TMJ and other joints warrants further investigation.[60–64]

This study had certain limitations. Additional time points with CT scans would be helpful for characterizing prosthesis deformation, or identifying locations where bone changes initiated. The structural integrity of the condyle was only examined after resection and may not provide an accurate reflection of *in vivo* relationships between TMJ structures. Although a biphasic scaffold was developed, only a bulk hydrogel was used here. Regenerating zonal cartilage architectures remains a goal for TMJ tissue engineering, although progress has been made with a bioreactor approach.[14] Hypothesis testing was not available due to the limited number of animals in this pilot study. A larger number of animals ($n = 6+$) may allow for hypothesis testing and statistical analysis for future investigations beyond this pilot study.

Conclusions

The results of this pilot study suggested improving bone continuity with the scaffold is a major goal for acellular TMJ condylar tissue engineering, which may require future efforts to consider cell seeding in the operating room and/or addition of biologic signals. An additional goal remains, improving cartilage regeneration with an integrated and layered structure like that of native condylar cartilage. Design features for resorbable scaffolds that could improve bone regeneration include adjustments to the porous architecture, load transmission profile, degradation rate, and use of biochemical signaling from growth factors (e.g., BMP-2) or peptides.

Acknowledgments

We would like to acknowledge generous contributions from the following, without whom this study would not have been possible: Dr. Emi Kiyotake, Chris Billings, Dr. Yingtao Liu, Dr. Shawn Lane, Courtney Rasbach, Dr. Hong Liu, Yuhua Li, Sheeja Aravindan, Dr. Reem Hossameldin, Dr. Adam Biedrzycki, Dave Samson, Mike Puccio, Ashley Potter, Dr. Jeremiah Easley, Jeannie Salash, Dr. Louis Mercuri, Dr. Jonathan Fillmore, Dr. David Hinkl, Dr. Shivakumar Raman, and Dr. Aaron Kotecki.

Authors' Contributions

D.S.N.: Methodology; conceptualization; formal analysis; software; and writing. A.R.: Methodology; formal analysis; and collect and analyze data. B.A.: Methodology. C.P.J.: Methodology and collect and analyze data. P.H.: Methodology and conceptualization. F.G.R.: Surgery; methodology; and writing-review and editing. W.R.W.: Methodology. K.-M.F.: Methodology. B.W.G.: Methodology. J.M.T.: Conceptualization and writing-review and editing. M.S.D.: Conceptualization and writing-review and editing.

Disclosure Statement

The authors have no conflicts of interest.

Funding Information

We thank the Osteo Science Foundation #10556980 for their generous support. Research reported in this publication was supported, in part, by the National Cancer Institute Cancer Center Support Grant P30CA225520 and COBRE P20GM103639 awarded to the University of Oklahoma Stephenson Cancer Center and used the Tissue Pathology Shared Resource. The content is solely the responsibility of the authors and does not necessarily represent the official views of the National Institutes of Health.

Supplementary Material

Supplementary Data S1
Supplementary Figure S1
Supplementary Table S1
Supplementary Video S1

References

1. Valesan LF, Da-Cas CD, Réus JC, et al. Prevalence of temporomandibular joint disorders: A systematic review and meta-analysis. Clin Oral Investig 2021;25(2):441–453; doi: 10.1007/s00784-020-03710-w
2. Anonymous. Prevalence of TMJD and Its Signs and Symptoms | National Institute of Dental and Craniofacial Research. n.d. Available from: https://www.nidcr.nih.gov/research/data-statistics/facial-pain/prevalence [Last accessed: March 26, 2023].

3. De Meurechy N, Braem A, Mommaerts MY. Biomaterials in temporomandibular joint replacement: Current status and future perspectives—a narrative review. Int J Oral Maxillofac Surg 2018;47(4):518–533; doi: 10.1016/j.ijom.2017.10.001
4. Sidebottom AJ. Current thinking in temporomandibular joint management. Br J Oral Maxillofac Surg 2009;47(2):91–94; doi: 10.1016/j.bjoms.2008.08.012
5. Mercuri L. Temporomandibular Joint Total Joint Replacement – TMJ TJR. Springer: Cham; 2016.
6. Louis G. Mercuri, Marco S. Caicedo. Material hypersensitivity and alloplastic temporomandibular joint replacement. J Oral Maxillofac Surg 2019;77(7):1371–1376; doi: https://doi.org/10.1016/j.joms.2019.01.042
7. Mercuri LG. Costochondral graft versus total alloplastic joint for temporomandibular joint reconstruction. Oral Maxillofac Surg Clin N Am 2018;30(3):335–342; doi: 10.1016/j.coms.2018.05.003
8. Detamore MS, Athanasiou KA, Mao J. A call to action for bioengineers and dental professionals: Directives for the future of TMJ bioengineering. Ann Biomed Eng 2007;35(8):1301–1311; doi: 10.1007/s10439-007-9298-6
9. Elledge R, Mercuri LG, Attard A, et al. Review of emerging temporomandibular joint total joint replacement systems. Br J Oral Maxillofac Surg 2019;57(8):722–728; doi: 10.1016/j.bjoms.2019.08.009
10. Wang L, Detamore MS. Tissue engineering the mandibular condyle. Tissue Eng 2007;13(8):1955–1971; doi: 10.1089/ten.2006.0152
11. Salash JR, Hossameldin RH, Almarza AJ, et al. Potential indications for tissue engineering in temporomandibular joint surgery. J Oral Maxillofac Surg 2016;74(4):705–711; doi: 10.1016/j.joms.2015.11.008
12. Almarza AJ, Brown BN, Arzi B, et al. Preclinical animal models for temporomandibular joint tissue engineering. Tissue Eng Part B Rev 2018;24(3):171–178; doi: 10.1089/ten.teb.2017.0341
13. Helgeland E, Shanbhag S, Pedersen TO, et al. Scaffold-Based Temporomandibular Joint Tissue Regeneration in Experimental Animal Models: A Systematic Review. An abstract of this article was presented as a poster, at The Bergen Stem Cell Consortium (BSCC), Annual meeting, Bergen, Norway, September 3–4, 2017. Tissue Eng Part B Rev 2018;24(4):300–316; doi: 10.1089/ten.teb.2017.0429
14. Chen D, Wu JY, Kennedy KM, et al. Tissue engineered autologous cartilage-bone grafts for temporomandibular joint regeneration. Sci Transl Med 2020;12(565):1–16.
15. Chin AR, Gao J, Wang Y, et al. Regenerative potential of various soft polymeric scaffolds in the temporomandibular joint condyle. J Oral Maxillofac Surg 2018;76(9):2019–2026; doi: 10.1016/j.joms.2018.02.012
16. Kalpakci KN, Willard VP, Wong ME, et al. An interspecies comparison of the temporomandibular joint disc. J Dent Res 2011;90(2):193–198; doi: 10.1177/0022034510381501
17. Bifano C, Hubbard G, Ehler W. A comparison of the form and function of the human, monkey, and goat temporomandibular joint. J Oral Maxillofac Surg 1994;52(3):272–275; doi: 10.1016/0278-2391(94)90298-4
18. Zhu S, Hu J, Li N, et al. Autogenous coronoid process as a new donor source for reconstruction of mandibular condyle: An experimental study on goats. Oral Surg Oral Med Oral Pathol Oral Radiol Endodontol 2006;101(5):572–580; doi: 10.1016/j.tripleo.2005.08.023
19. Hagandora CK, Chase TW, Almarza AJ. A Comparison of the Mechanical Properties of the Goat Temporomandibular Joint Disc to the Mandibular Condylar Cartilage in Unconfined Compression. J Dent Biomech 2011;2011:212385; doi: 10.4061/2011/212385
20. Abramowicz S, Crotts SJ, Hollister SJ, et al. Tissue-engineered vascularized patient-specific temporomandibular joint reconstruction in a Yucatan pig model. Oral Surg Oral Med Oral Pathol Oral Radiol 2021;132(2):145–152; doi: 10.1016/j.oooo.2021.02.002
21. Dormer NH, Busaidy K, Berkland CJ, et al. Osteochondral interface regeneration of rabbit mandibular condyle with bioactive signal gradients. J Oral Maxillofac Surg 2011;69(6):e50–e57; doi: 10.1016/j.joms.2010.12.049
22. Weng Y, Cao Y, Arevalo C, et al. Tissue-engineered composites of bone and cartilage for mandible condylar reconstruction. J Oral Maxillofac Surg 2001;59(2):185–190; doi: 10.1053/joms.2001.20491
23. Athanasiou KA, Almarza AA, Detamore MS, et al. Tissue Engineering of Temporomandibular Joint Cartilage. Synthesis Lectures on Tissue Engineering. Springer International Publishing: Cham; 2009.
24. Hollister S, Lin C, Saito E, et al. Engineering craniofacial scaffolds. Orthod Craniofac Res 2005;8(3):162–173; doi: 10.1111/j.1601-6343.2005.00329.x
25. Beck EC, Barragan M, Libeer TB, et al. Chondroinduction from naturally derived cartilage matrix: A comparison between devitalized and decellularized cartilage encapsulated in hydrogel pastes. Tissue Eng Part A 2016;22(7–8):665–679; doi: 10.1089/ten.tea.2015.0546
26. Kiyotake EA, Cheng ME, Thomas EE, et al. The rheology and printability of cartilage matrix-only biomaterials. Biomolecules 2022;12(6):846; doi: 10.3390/biom12060846
27. Townsend JM, Sanders ME, Kiyotake EA, et al. Independent control of molecular weight, concentration, and stiffness of hyaluronic acid hydrogels. Biomed Mater 2022;17(6):065005; doi: 10.1088/1748-605X/ac8e41
28. Nedrelow DS, Townsend JM, Detamore MS. The ogden model for hydrogels in tissue engineering: Modulus determination with compression to failure. J Biomech 2023;152:111592; doi: 10.1016/j.jbiomech.2023.111592
29. Kiyotake EA, Douglas AW, Thomas EE, et al. Development and quantitative characterization of the precursor rheology of hyaluronic acid hydrogels for bioprinting. Acta Biomater 2019;95:176–187; doi: 10.1016/j.actbio.2019.01.041
30. van den Borne MPJ, Raijmakers NJH, Vanlauwe J, et al. International Cartilage Repair Society (ICRS) and Oswestry macroscopic cartilage evaluation scores validated for use in Autologous Chondrocyte Implantation (ACI) and microfracture. Osteoarthritis Cartilage 2007;15(12):1397–1402; doi: 10.1016/j.joca.2007.05.005
31. Vapniarsky N, Simpson DL, Arzi B, et al. Histological, immunological, and genetic analysis of feline chronic gingivostomatitis. Front Vet Sci 2020;7:310; doi: 10.3389/fvets.2020.00310
32. Ma J, Lin L, Zuo Y, et al. Modification of 3D printed PCL scaffolds by PVAc and HA to enhance cytocompatibility

and osteogenesis. RSC Adv 2019;9(10):5338–5346; doi: 10.1039/C8RA06652C
33. Cao C, Huang P, Prasopthum A, et al. Characterisation of bone regeneration in 3D printed ductile PCL/PEG/hydroxyapatite scaffolds with high ceramic microparticle concentrations. Biomater Sci 2022;10(1):138–152; doi: 10.1039/D1BM01645H
34. Ebrahimi Z, Irani S, Ardeshirylajimi A, et al. Enhanced osteogenic differentiation of stem cells by 3D printed PCL scaffolds coated with collagen and hydroxyapatite. Sci Rep 2022;12(1):12359; doi: 10.1038/s41598-022-15602-y
35. Greco F, Leonetti L, Pranno A, et al. Mechanical behavior of bio-inspired nacre-like composites: A hybrid multiscale modeling approach. Compos Struct 2020;233:111625; doi: 10.1016/j.compstruct.2019.111625
36. Erkliğ A, Alsaadi M, Bulut M. A comparative study on industrial waste fillers affecting mechanical properties of polymer-matrix composites. Mater Res Express 2016; 3(10):105302; doi: 10.1088/2053-1591/3/10/105302
37. Saldívar MC, Doubrovski EL, Mirzaali MJ, et al. Nonlinear coarse-graining models for 3D printed multi-material biomimetic composites. Addit Manuf 2022;58:103062; doi: 10.1016/j.addma.2022.103062
38. Nickel JC, Iwasaki LR, Gonzalez YM, et al. Mechanobehavior and ontogenesis of the temporomandibular joint. J Dent Res 2018;97(11):1185–1192; doi: 10.1177/0022034518786469
39. Boyd RL, Gibbs CH, Mahan PE, et al. Temporomandibular joint forces measured at the condyle of Macaca arctoides. Am J Orthod Dentofacial Orthop 1990;97(6):472–479; doi: 10.1016/S0889-5406(05)80027-7
40. Sumner DR. Long-term implant fixation and stress-shielding in total hip replacement. J Biomech 2015;48(5): 797–800; doi: 10.1016/j.jbiomech.2014.12.021
41. Ramos A, Mesnard M. A new condyle implant design concept for an alloplastic temporomandibular joint in bone resorption cases. J Cranio-Maxillofac Surg 2016;44(10): 1670–1677; doi: 10.1016/j.jcms.2016.07.024
42. Ko C-C, Swift JQ, DeLong R, et al. An intra-oral hydraulic system for controlled loading of dental implants. J Biomech 2002;35(6):863–869; doi: 10.1016/S0021-9290(02)00004-0
43. Szmukler-Moncler S, Salama H, Reingewirtz Y, et al. Timing of loading and effect of micromotion on bone-dental implant interface: Review of experimental literature. J Biomed Mater Res 1998;43(2):192–203; doi: 10.1002/(SICI)1097-4636(199822)43:2<192::AID-JBM14>3.0.CO;2-K
44. Wolford LM, Mercuri LG, Schneiderman ED, et al. Twenty-year follow-up study on a patient-fitted temporomandibular joint prosthesis: The techmedica/TMJ concepts device. J Oral Maxillofac Surg 2015;73(5):952–960; doi: 10.1016/j.joms.2014.10.032
45. Granquist EJ, Bouloux G, Dattilo D, et al. Outcomes and survivorship of biomet microfixation total joint replacement system: Results from an FDA postmarket study. J Oral Maxillofac Surg 2020;78(9):1499–1508; doi: 10.1016/j.joms.2020.04.021
46. Paluch EK, Nelson CM, Biais N, et al. Mechanotransduction: Use the force(s). BMC Biol 2015;13(1):47; doi: 10.1186/s12915-015-0150-4
47. Meslier QA, Shefelbine SJ. Using finite element modeling in bone mechanoadaptation. Curr Osteoporos Rep 2023;21(2):105–116; doi: 10.1007/s11914-023-00776-9
48. Shefelbine SJ, Carter DR. Mechanobiological predictions of growth front morphology in developmental hip dysplasia. J Orthop Res 2004;22(2):346–352; doi: 10.1016/j.orthres.2003.08.004
49. Stelea CG, Agop-Forna D, Dragomir R, et al. Recovery of post-traumatic temporomandibular joint after mandibular fracture immobilization: A literature review. Appl Sci 2021;11(21):10239; doi: 10.3390/app112110239
50. Franklin M, Sperry MM, Phillips E, et al. Painful temporomandibular joint overloading induces structural remodeling in the pericellular matrix of that joint's chondrocytes. J Orthop Res 2022;40(2):348–358; doi: 10.1002/jor.25050
51. Chen J, Sorensen KP, Gupta T, et al. Altered functional loading causes differential effects in the subchondral bone and condylar cartilage in the temporomandibular joint from young mice. Osteoarthritis Cartilage 2009;17(3):354–361; doi: 10.1016/j.joca.2008.05.021
52. Lanza R, Atala A, (eds). Essentials of Stem Cell Biology. 3rd ed. Elsevier: Waltham, MA; 2014.
53. Detamore MS, Hegde JN, Wagle RR, et al. Cell type and distribution in the porcine temporomandibular joint disc. J Oral Maxillofac Surg 2006;64(2):243–248; doi: 10.1016/j.joms.2005.10.009
54. Bi R, Yin Q, Li H, et al. A single-cell transcriptional atlas reveals resident progenitor cell niche functions in TMJ disc development and injury. Nat Commun 2023;14(1):830; doi: 10.1038/s41467-023-36406-2
55. Donahue ND, Acar H, Wilhelm S. Concepts of nanoparticle cellular uptake, intracellular trafficking, and kinetics in nanomedicine. Adv Drug Deliv Rev 2019;143:68–96; doi: 10.1016/j.addr.2019.04.008
56. Ruscitto A, Scarpa V, Morel M, et al. Notch regulates fibrocartilage stem cell fate and is upregulated in inflammatory TMJ arthritis. J Dent Res 2020;99(10):1174–1181; doi: 10.1177/0022034520924656
57. Simeonov KP, Byrns CN, Clark ML, et al. Single-cell lineage tracing of metastatic cancer reveals selection of hybrid EMT states. Cancer Cell 2021;39(8):1150–1162.e9; doi: 10.1016/j.ccell.2021.05.005
58. Nettleton K, Luong D, Kleinfehn AP, et al. Molecular mass-dependent resorption and bone regeneration of 3D printed PPF scaffolds in a critical-sized rat cranial defect model. Adv Healthc Mater 2019;8(17):1900646; doi: 10.1002/adhm.201900646
59. Polak SJ, Rustom LE, Genin GM, et al. A mechanism for effective cell-seeding in rigid, microporous substrates. Acta Biomater 2013;9(8):7977–7986; doi: 10.1016/j.actbio.2013.04.040
60. Monteiro JLGC, Guastaldi FPS, Troulis MJ, et al. Induction, treatment, and prevention of temporomandibular joint ankylosis—A systematic review of comparative animal studies. J Oral Maxillofac Surg 2021;79(1):109–132.e6; doi: 10.1016/j.joms.2020.07.018
61. Ruggiero L, Zimmerman BK, Park M, et al. Roles of the fibrous superficial zone in the mechanical behavior of TMJ condylar cartilage. Ann Biomed Eng 2015;43(11):2652–2662; doi: 10.1007/s10439-015-1320-9
62. Yang K, Wang HL, Dai Y-M, et al. Which of the fibrous layer is more important in the genesis of traumatic temporomanibular joint ankylosis: The mandibular condyle

or the glenoid fossa? J Stomatol Oral Maxillofac Surg 2020;121(5):517–522; doi: 10.1016/j.jormas.2019.12.014
63. Yan Y-B, Li J-M, Xiao E, et al. A pilot trial on the molecular pathophysiology of traumatic temporomandibular joint bony ankylosis in a sheep model. Part II: The differential gene expression among fibrous ankylosis, bony ankylosis and condylar fracture. J Cranio-Maxillofac Surg 2014;42(2):e23–e28; doi: 10.1016/j.jcms.2013.04.008
64. Miyamoto H, Kurita K, Ogi N, et al. The role of the disk in sheep temporomandibular joint ankylosis. Oral Surg Oral Med Oral Pathol Oral Radiol Endodontol 1999;88(2):151–158; doi: 10.1016/S1079-2104(99)70109-5

Address correspondence to:
Michael S. Detamore, PhD
Stephenson School of Biomedical Engineering
University of Oklahoma
Norman, OK 73019
USA

E-mail: detamore@ou.edu

Received: April 26, 2023
Accepted: June 1, 2023
Online Publication Date: July 18, 2023